Systematic Electron Crystallographic Studies of Self-Assembled Binary Nanocrystal Superlattices

Jun Chen,[†,§] Xingchen Ye,[‡,§] and Christopher B. Murray[†,‡,*]

[†]Department of Materials Science and Engineering and [‡]Department of Chemistry, University of Pennsylvania, Philadelphia, Pennsylvania 19104. [§]These authors contributed equally to this work.

ABSTRACT Multicomponent nanocrystal assemblies have received great attention due to their fundamental role in the study of self-assembly and novel physical properties arising from particle interactions. Here, we report the formation of the first binary nanocrystal superlattices (BNSLs) consisting of different-sized Fe_3O_4 nanocrystals. We establish a framework to systematically study the structure of BNSLs using a dual-axis tomography TEM holder. The tilt series obtained not only allows us to map the three-dimensional (3D) structure of icosahdedral AB_{13} (ico-AB_{13}) and AlB_2-type BNSLs but also uncovers the structural differences among the projections of ico-AB_{13}, cuboctahedral AB_{13} (cub-AB_{13}), and AlB_2. This structural characterization method is general and is important for further exploration of structural diversity in BNSLs and in the development of rigorous structure—property relationships in BNSLs. The formation of ico-AB_{13} and AlB_2 BNSLs from electrostatically neutral Fe_3O_4 nanoparticles is consistent with the space-filling principles and further supports entropy as the dominant factor during the growth of these BNSLs.

*Address correspondence to cbmurray@sas.upenn.edu.

Colloidal "bottom-up" assembly of nanoscale building blocks into well-ordered superlattices offers tremendous potential for their applications in electrical, optical, and magnetic devices.[1−12] Recently, a variety of BNSLs were investigated in metallic—metallic,[13,14] semiconductor—magnetic,[15] semiconductor—semiconductor,[16,17] metallic—semiconductor,[18] metallic—magnetic,[19−22] and magnetic—magnetic[23,24] nanocrystal (NC) combinations, exhibiting a diverse array of crystal structures. Synergistic effects arising from particle interactions have been reported in several multicomponent nanocrystal assemblies.[25−27] For example, AB-type binary PbTe—Ag_2Te nanocrystal superlattices show strongly enhanced p-type electronic conductivity.[25] Fe_3O_4 and FePt nanocrystal composites show enhanced energy density due to magnetic exchange coupling.[26] Therefore, engineering the three-dimensional (3D) structures of BNSLs by placing different NCs in a well-defined geometry offers a promising route for tailoring the collective properties of the nanostructured architectures.

TEM has been widely used in the structural analysis of self-assembled nanocrystal superlattices.[28,29] However, the structural assignments of BNSLs have been mainly based on the visual comparison of TEM images with the projections of known crystal structures. Only a few examples have taken advantage of electron-diffraction-based techniques combined with real-space imaging in the structural characterization of BNSLs.[15,18] Here, we employ a dual-axis tomography TEM holder to systematically study the 3D crystal structure of BNSLs. We highlight the effectiveness of the 3D crystallography approach in the studies of AB_{13}-type BNSLs where two polymorphs have been proposed.[18] We are able to obtain 9 different tilt series and identify 14 distinct crystallographic projections from the AB_{13}-type BNSLs. The TEM holder's in-plane 360° rotation function allows us to align a particular crystallographic direction parallel to the holder's tilt axis before each tilt series is started. Through careful analysis of TEM images and corresponding small-angle electron diffraction (ED) patterns from each tilt series, we confirm that the Fe_3O_4—Fe_3O_4 AB_{13}-type BNSLs in this study can be assigned uniquely to the ico-AB_{13} type.

The ico-AB_{13} phase (space group $F m\bar{3}c$, No. 226) was initially identified in $NaZn_{13}$ and several other intermetallic compounds[30,31] and is theoretically predicted to be stable based on the hard sphere approximation.[32] It was also observed in naturally occurring opals (colloidal crystals),[32−35] C_{60}—CCl_4 solvate crystals,[36] and binary mixtures of block
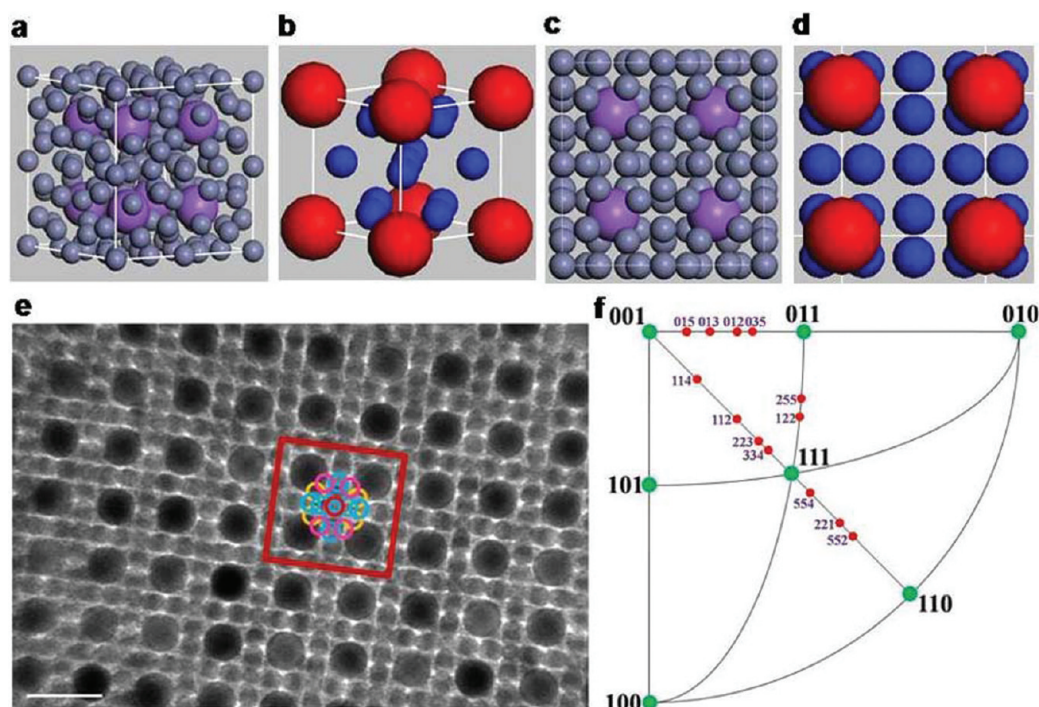
Figure 1. Structural models and stereographic projection of AB$_{13}$ BNSLs. Unit cells of (a) ico-AB$_{13}$ and (b) cub-AB$_{13}$ structures. Structural models of [001] projections of (c) ico-AB$_{13}$ and (d) cub-AB$_{13}$ structures. (e) TEM image of [001] projection of ico-AB$_{13}$ BNSLs composed of 5.6 and 10.5 nm Fe$_3$O$_4$ NCs. The inset shows detailed nanocrystal arrangement of the [001] projection. The scale bar is 20 nm. (f) Stereographic projection of the cubic crystal system. The projection plane is normal to the [001] direction.

copolymer micelles.[37] The unit cell of the ico-AB$_{13}$ structure (Figure 1a) contains 104 small spheres and 8 large spheres. The structure can be viewed in the following way: an icosahedron consisting of 13 small spheres inside a simple cubic lattice of large spheres. The orientation of adjacent icosahedra is rotated by 90°. An alter-
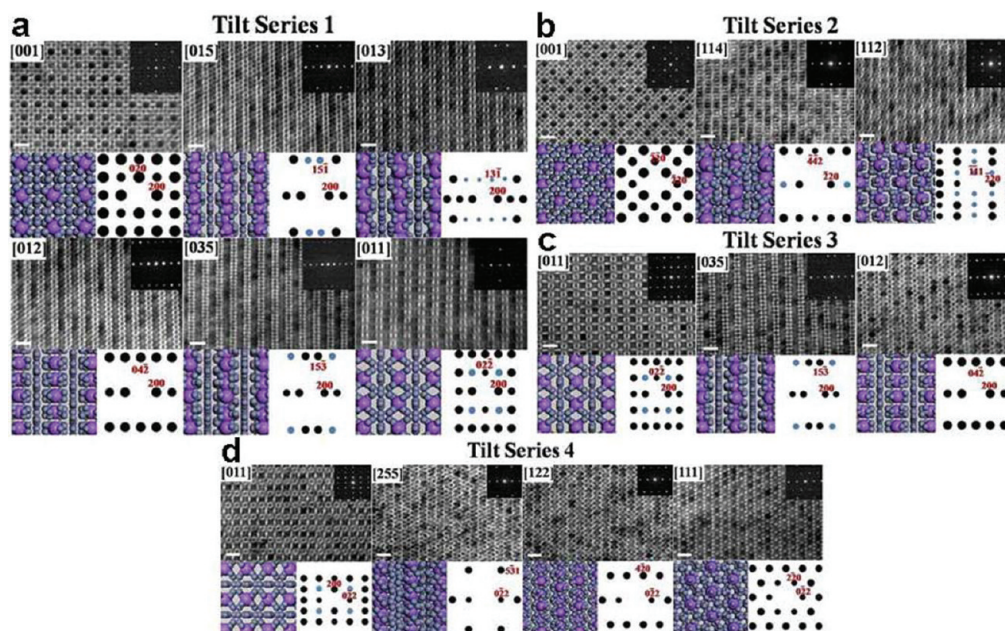

Figure 2. Tilt series 1−4 of ico-AB$_{13}$ BNSLs composed of 5.6 and 10.5 nm Fe$_3$O$_4$ NCs. Below each TEM image (inset of each is the corresponding small-angle ED pattern) are the corresponding structural model (left) and simulated ED pattern (right). The blue spots of the simulated ED patterns are kinematically forbidden reflections but could appear experimentally due to secondary diffraction. (a) Tilt series 1 starts from [001] zone axis and tilts around [100] direction. Tilting sequence: [001] → [015] → [013] → [012] → [035] → [011] zone axes. (b) Tilt series 2 starts from [001] zone axis and tilts around [110] direction. Tilting sequence: [001] → [114] → [112] zone axes. (c) Tilt series 3 starts from [011] zone axis and tilts around [100] direction. Tilting sequence: [011] → [035] → [012] zone axes. (d) Tilt series 4 starts from [011] zone axis and tilts around [0$\bar{1}$1] direction. Tilting sequence: [011] → [255] → [122] → [111] zone axes. All scale bars are 20 nm.
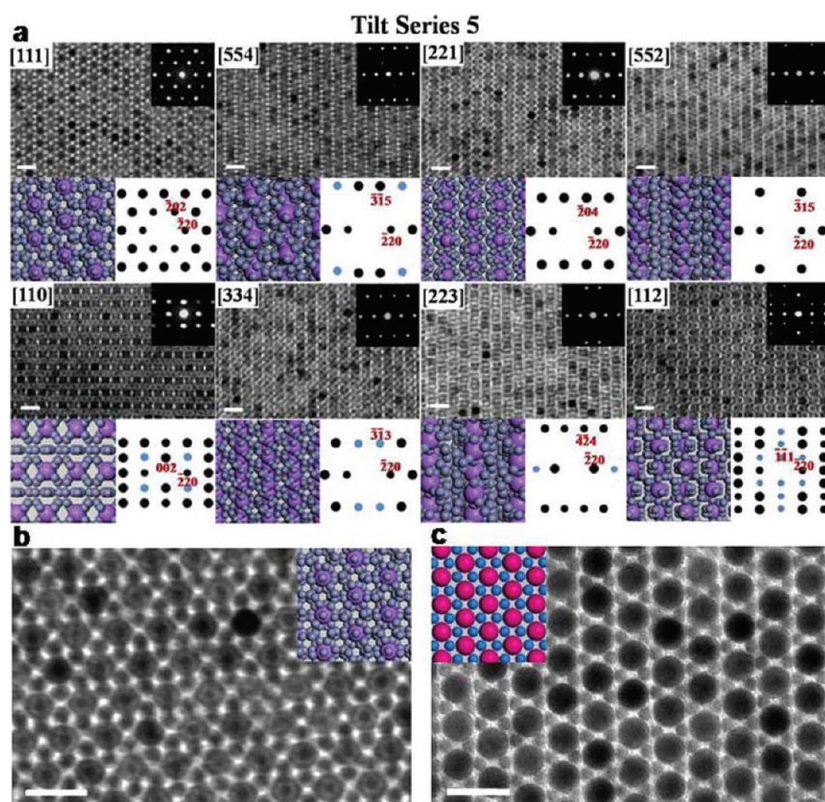
Tilt Series 5

Figure 3. Tilt series 5 of ico-AB$_{13}$ BNSLs composed of 5.6 and 10.5 nm Fe$_3$O$_4$ NCs and structural comparison between ico-AB$_{13}$ and AlB$_2$ type BNSLs. (a) Tilt series 5 starts from [111] zone axis and tilts around [$\bar{1}$10] direction. Tilting sequence: [111] → [554] → [221] → [552] → [110] and [111] → [334] → [223] → [112] zone axes. The blue spots are kinematically forbidden reflections but could appear experimentally due to secondary diffraction. Below each TEM image (inset of each is the corresponding small-angle ED pattern) are the corresponding structural model (left) and simulated ED pattern (right). The blue spots of the simulated ED patterns are kinematically forbidden reflections but could appear experimentally due to secondary diffraction. (b) TEM image of [111] projection of ico-AB$_{13}$ Fe$_3$O$_4$ BNSLs. The inset is the structural model of the [111] projection of ico-AB$_{13}$. (c) TEM image of the [001] projection of AlB$_2$ BNSLs assembled from 5.6 and 10.5 nm Fe$_3$O$_4$ NCs. The inset is the structural model of the [001] projection of AlB$_2$. All scale bars are 20 nm.

red, eight blue, and four yellow circles belong to a subcell, while the other four pink circles are from an adjacent subcell) can be clearly resolved inside a simple cubic lattice formed by eight large NCs, as shown in the inset of Figure 1e. Importantly, the partial overlap between each pair of the blue circles uniquely matches the [001] projection of the ico-AB$_{13}$ structural model (Figure 1c). In contrast, the [001] projection of cub-AB$_{13}$ structural model (Figure 1d) shows that only nine small NCs inside a simple cubic unit cell can be seen. We caution that, at low magnification, it is difficult to distinguish between ico-AB$_{13}$ and cub-AB$_{13}$ structure from the [001] projection due to their subtle structural differences.

In BNSLs, usually domains with different orientations coexist in the same sample. To ascertain whether they belong to different crystal structures or different zone axes of the same crystal structure, it is necessary to acquire series tilt from different domains of the sample. According to the stereographic projection of cubic crystal system shown in Figure 1f, we design a set of series tilt paths which include as many low index zone axes as possible.[39]

Starting from a [001]-oriented domain, two different tilt paths are chosen: the first one (Figure 2a) tilts around the [100] direction, heading toward the [011] zone axis. After 45° in-plane rotation of the same [001] domain, the second tilt series (Figure 2b) starts by tilting around the [$\bar{1}$10] direction and proceeds toward the [111] zone axis. Starting from a [011]-oriented domain, we also have two choices: one is targeted at the [001] zone axis as shown in the third tilt series (Figure 2c). The [035] and [012] zone axes appear again, which confirms that the first and third tilt series are along the same path but in opposite direction (Figure 1f). Moreover, after 90° in-plane rotation of the same [011] domain, the fourth tilt series (Figure 2d) proceeds toward the [111] projection, during which the TEM images taken along the [255] and the [122] zone axes are identified according to the small-angle ED patterns. The [111] projection may be confused with either the [111] projection of cub-AB$_{13}$ or the [001] projection of the AlB$_2$ type (space group $P6/mmm$, No. 191) BNSLs since all of the corresponding small-angle ED patterns have six-fold symmetry. Therefore, we find several untilted domains analogous to the [111] projection of ico-AB$_{13}$ and do both positive-angle and negative-angle series tilt around the [$\bar{1}$10] direction.

native cub-AB$_{13}$ phase (space group $Pm\bar{3}m$, No. 221) was proposed as a polymorph, although it is structurally unfavorable based on hard sphere packing density calculations.[32] It differs from the ico-AB$_{13}$ in the following manner: 8 large spheres are located at the corners of a simple cubic lattice inside which 12 small spheres occupy the vertices of a virtual cuboctahedron, surrounding a central small sphere (Figure 1b). Therefore, the two AB$_{13}$ polymorphs differ in the arrangement of small spheres and, thus, in their packing density and symmetry (face-centered cubic *vs* simple cubic). The first ico-AB$_{13}$ BNSLs were reported in 2003.[15] Interestingly, there have been several subsequent reports of the formation of both ico-AB$_{13}$[16,18,20,21,38] and cub-AB$_{13}$ BNSLs.[16−18,20,21,27] Factors such as van der Waals (VDW) interactions, dipolar forces, *etc.* have been taken into account to explain the growth mechanism of cub-AB$_{13}$ BNSLs; however, a consensus on the predominant interaction has not been reached.

The [001] projection, which is commonly observed in AB$_{13}$-type BNSLs, is shown in Figure 1e. Seventeen small NCs (marked by colored circles: one
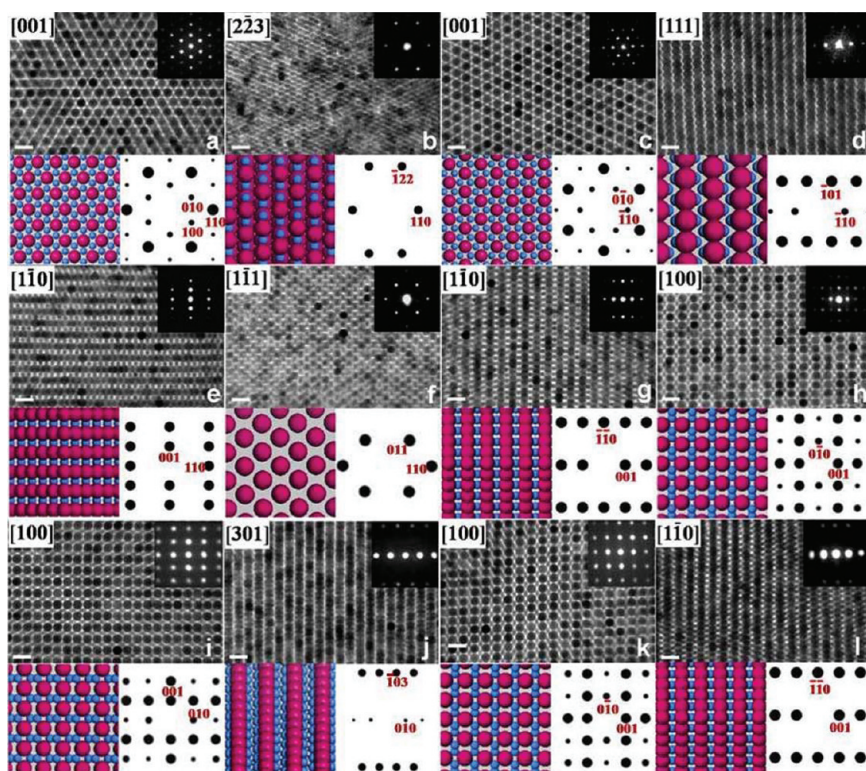
Figure 4. Six tilt series of AlB$_2$ BNSLs composed of 5.6 and 10.5 nm Fe$_3$O$_4$ NCs. Below each TEM image (inset of each is the corresponding small-angle ED pattern) are the corresponding structural model (left) and simulated ED pattern (right). Tilt series 1 (a,b) starts from [001] zone axis, tilts around [110] direction, and ends up at [2$\bar{2}$3] zone axis. After 90° in-plane rotation of (a), tilt series 2 (c,d) starts from [001] zone axis, tilts around [$\bar{1}$10] direction, and ends up at [111] zone axis. Tilt series 3 (e,f) starts from [1$\bar{1}$0] zone axis, tilts around [110] direction, and ends up at [1$\bar{1}$1] zone axis. After 90° in-plane rotation of (e), tilt series 4 (g,h) starts from [1$\bar{1}$0] zone axis, tilts around [001] direction, and ends up at [100] zone axis. Tilt series 5 (i,j) starts from [100] zone axis, tilts around [010] direction, and ends up at [$\bar{3}$01] zone axis. After 90° in-plane rotation of (i), tilt series 6 (k,l) starts from [100] zone axis, tilts around [001] direction, and ends up at [1$\bar{1}$0] zone axis. All scale bars are 20 nm.

Typical results are shown in Figure 3a: [221] and [552] projections, equivalent to the [122] and [255] projections, respectively, "re-appear" as we tilt the BNSLs and finally the [110] projection is reached. Interestingly, in
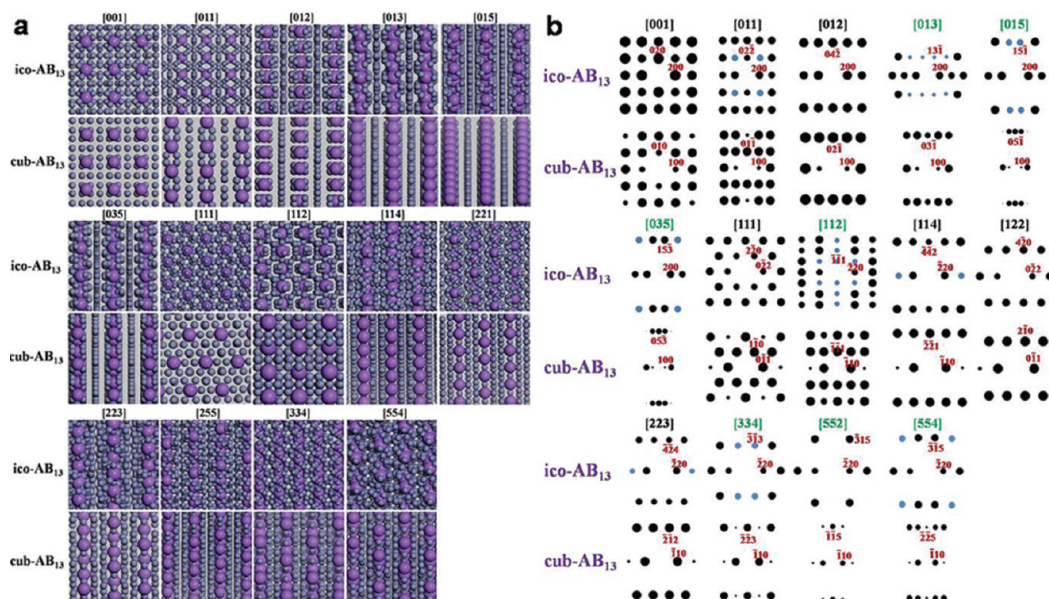

Figure 5. Crystal structural modeling and electron diffraction simulation of AB$_{13}$ structures. (a) Structural models of different projections of ico-AB$_{13}$ and cub-AB$_{13}$ structures. (b) Simulated ED patterns of different zone axes of ico-AB$_{13}$ and cub-AB$_{13}$ structures using EMS software. The ED patterns of ico-AB$_{13}$ and cub-AB$_{13}$ are different in the following seven zone axes (green): [013], [015], [035], [112], [334], [552], and [554]. The blue spots are kinematically forbidden reflections but could appear experimentally due to secondary diffraction.
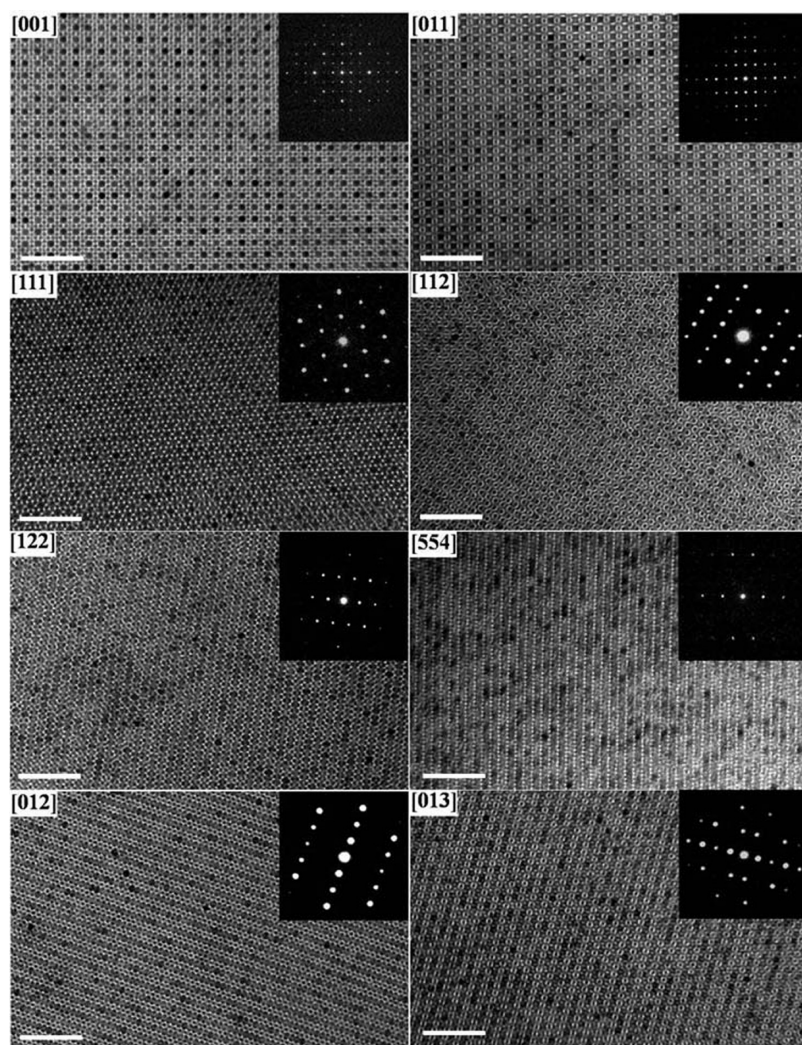
Figure 6. Large-area TEM images of different projections in ico-AB$_{13}$ BNSLs composed of 5.6 and 10.5 nm Fe$_3$O$_4$ NCs. TEM images and small-angle ED patterns (inset) of Fe$_3$O$_4$–Fe$_3$O$_4$ ico-AB$_{13}$ BNSLs from different domains. All scale bars are 100 nm.

in contrast to the [001] projection of the AlB$_2$ structure (Figure 3c). However, a series tilt from this projection is more definitive for the structural identification.

During the five tilt series of AB$_{13}$-type BNSLs (Figures 2 and 3), several intermediate zone axes appear such as [012], [013], [221], [554], *etc*. The fact that they are along the pathway connecting those low-index poles ([001], [011], and [111]) on the stereographic projection motivates us to start tilting from these projections to see whether we could end up with one of the low-index zone axes. Starting from [012]-, [013]-, [221]-,and [554]-oriented domains, we are able to reach the [001], [011], and [111] poles, as shown in tilt series 6–9 (Figures S1–S4 in Supporting Information). The correspondence between TEM images and structural models and between small-angle ED and the simulated patterns confirms that the AB$_{13}$ Fe$_3$O$_4$–Fe$_3$O$_4$ BNSLs are exclusively ico-AB$_{13}$. We also simulate ED patterns (Figure 5b) of cub-AB$_{13}$ structure and find that ico-AB$_{13}$ and cub-AB$_{13}$ cannot be differentiated based solely on the ED patterns of the following seven zone axes: [001], [011], [012], [111], [114], [122], and [223], while discrepancies do occur in the other seven zone axes: [013], [015], [035], [112], [334], [552], and [554]. This further supports our structural assignment of ico-AB$_{13}$ rather than cub-AB$_{13}$.

After analyzing many (>200) Fe$_3$O$_4$–Fe$_3$O$_4$ ico-AB$_{13}$ BNSLs formed under similar deposition conditions, we find that eight projections are commonly seen in ico-AB$_{13}$ samples (Figure 6). Several projections show characteristic contrast under TEM; besides the above-mentioned wave-like [112] projection, the [011] and [013] projections show an "eye-like" feature. The difference between [122] and [012], as seen in Figure 6, can be visualized by the number of small nanocrystal chains around each large nanocrystal chain (four *vs* two). Statistically, [001]- and [011]-oriented domains are more likely to be observed, which indicates preferential orientation in the BNSL growth. Typical large-area views of the [001] and [011] projections are shown in Figures S5 and S6 (Supporting Information). The ico-AB$_{13}$ BNSLs typically exhibit a mosaic texture with sharp grain boundaries separating oriented domains, islands that nucleate and coalesce during the BNSLs growth process (Figure S7).

The formation of large-area (up to 100 μm^2) ico-AB$_{13}$ Fe$_3$O$_4$–Fe$_3$O$_4$ BNSLs is due to the monodispersity (size and shape) of the individual building blocks (Figures S8–S10). Both 12.7–7.4 and 16.3–9.3 nm (here

the reverse tilting direction, we end up with the [112] projection with its characteristic wave-like contrast. The small-angle ED matches with the simulated [112] pattern. A structural model built from Accelrys Materials Studio 4.4 software displays the same wavy modulation, which is absent in the simulated [112] projection based on cub-AB$_{13}$ (Figure 5a). This is strong evidence that the starting point of the fifth tilt series is the [111] projection of the ico-AB$_{13}$ structure. The movies for tilt series 1–5 using 7.3 and 14.5 nm Fe$_3$O$_4$–Fe$_3$O$_4$ ico-AB$_{13}$ BNSLs are shown in Supporting Information (movies S1–S5).

By adjusting the concentration ratio of 5.6 to 10.5 nm Fe$_3$O$_4$ NCs, AlB$_2$ structure can also be obtained. Series tilt starting from the [001]-oriented domain of the AlB$_2$ structure is shown in Figure 4. It should be pointed out that the difference between the [111] projection of ico-AB$_{13}$ and the [001] projection of the AlB$_2$ structure can be seen in the following way: In Figure 3b, there is one small nanocrystal sitting on top of each large nanocrystal in the [111] projection of the ico-AB$_{13}$ structure,
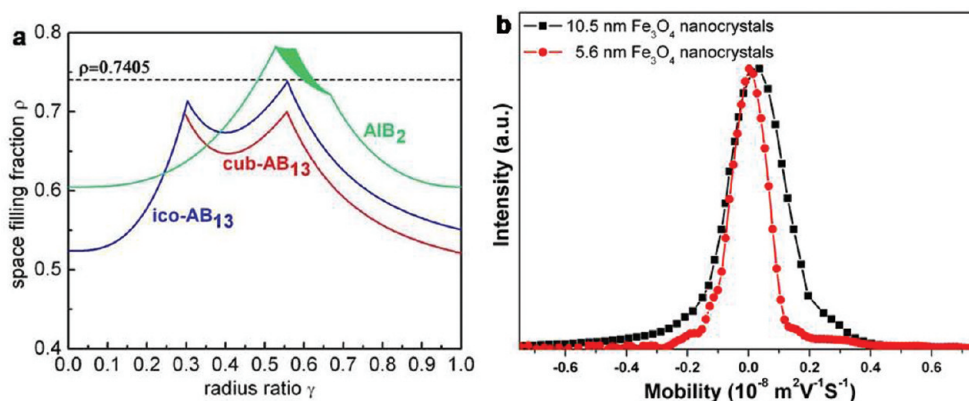
Figure 7. (a) Space-filling curves of ico-AB_{13}, cub-AB_{13}, and AlB_2 structures. The black dashed line represents the packing density $\rho = 0.7405$ of the single-component close-packed structures. The filled-in section in the AlB_2 curve corresponds to different arrangements of densely packed spheres. **(b)** Electrophoretic mobility of two different-sized Fe_3O_4 nanocrystals dispersed in trichloroethylene.

we refer to the effective sizes of nanocrystals which includes the thickness of surface ligands)[21] combinations give rise to a size ratio (γ) close to 0.58. Previous theoretical work demonstrated that binary mixtures of colloidal particles with $\gamma = 0.58$ entropically (space-filling) favor the formation of either AB_{13} or AB_2 superlattice structures, depending on the relative concentration of the two species[35,40] (Figure 7a). Recently, it was proposed that not only entropy but also other factors such as VDW, dipolar, and Coulombic interactions should also be taken into account. For example, the recent report on $CaCu_5$-type BNSLs shows that even certain structures unfavorable based on the space-filling principle can form, suggesting that the contribution from VDW interaction of interdigitating ligands is important.[16] On the other hand, 3D binary superlattices of oppositely charged colloids have been successfully demonstrated and explained in terms of balance between entropic and Coulombic interactions.[41−43] In our case, the Fe_3O_4 NCs stabilized with oleic acid molecules are confirmed to be electrostatically neutral by ζ potential measurements (Figure 7b), similar to the reported CdTe−CdSe system.[16] Therefore, we believe that the formation of our ico-AB_{13} and AlB_2 BNSLs is mainly entropy-driven.

In summary, ico-AB_{13} and AlB_2 BNSLs consisting of 5.6 nm Fe_3O_4 and 10.5 nm Fe_3O_4, as well as 7.3

nm Fe_3O_4 and 14.5 nm Fe_3O_4 nanocrystals were assembled. We have developed a systematic method to characterize the 3D structure of BNSLs; we use stereographic projection as a standard crystallographic tool to design series tilt paths and to index crystal zone axes. Series tilt using a dual-axis tomography holder allows acquisition of TEM images and small-angle ED patterns while establishing structural correlations among different domains of the BNSLs. This systematic crystallography study confirms the unique assignment of ico-AB_{13} rather than cub-AB_{13} in these $Fe_3O_4-Fe_3O_4$ BNSLs. A library of TEM images and small-angle ED patterns of ico-AB_{13} and AlB_2 BNSLs as well as the structural models and simulated ED diffraction patterns is provided as resources for future phase identification of ico-AB_{13}, cub-AB_{13}, and AlB_2 structures assembled from any combination of nanocrystal building blocks. Nanocrystal superlattices not only provide opportunities to study fundamental particle interactions but also offer the possibility to capture and harness emergent properties. Systematic 3D structural characterization is essential for further exploration of structural diversity and structure−property relationships in multicomponent nanoscale assemblies.

METHODS

Synthesis and Characterization of Fe_3O_4 Nanocrystals. The Fe_3O_4 nanocrystals were synthesized using the method developed by Hyeon et al.[44] Briefly, iron oleate precursor was prepared by the reaction of 10.8 g of iron(III) chloride and 36.5 g of sodium oleate at 60 °C for 4 h. The 10.5 nm Fe_3O_4 nanocrystals were synthesized by dissolving 3.6 g of iron oleate and 1.28 mL of oleic acid in 20 mL of 1-octadecene, which was then heated to 320 °C at a rate of 3 °C/min and kept at 320 °C for 30 min. After cooling to room temperature, ethanol was added to the crude solution to precipitate Fe_3O_4 nanocrystals and remove reaction byproducts. Fe_3O_4 nanocrystals of other sizes are obtained by adjusting the ratio of oleic acid

to iron oleate. All Fe_3O_4 nanocrystals were redispersed in trichloroethylene (TCE) with a nanocrystal concentration about 1.5 mg/mL. Electrophoretic mobility measurements were performed on a Delsa Nano C system (Beckman Coulter).

Preparation of Binary Nanocrystal Superlattices. A TEM grid (300 mesh, Electron Microscopy Sciences) was placed at the bottom of a glass vial containing TCE solution of two different-sized Fe_3O_4 nanocrystals. For AB_{13} BNSLs, the binary nanocrystal solution was made by adding 20 μL of 5.6 nm (7.3 nm) Fe_3O_4 nanocrystals and 10 μL of 10.5 nm (14.5 nm) Fe_3O_4 nanocrystals into 100 μL of TCE. For AB_2 BNSLs, the binary nanocrystal solution was made by adding 10 μL of 5.6 nm

(7.3 nm) Fe_3O_4 nanocrystals and 30 μL of 10.5 nm (14.5 nm) Fe_3O_4 nanocrystals into 100 μL of TCE. The vial was tilted by 45° inside a vacuum oven under reduced pressure (∼30 kPa) at 50 °C. The grid was taken out after 12 h for further structural analysis.

Structural Characterization of Binary Nanocrystal Superlattices. TEM images and electron diffraction patterns were taken on a JEM-1400 transmission electron microscope equipped with a SC 1000 ORIUS CCD camera operating at 120 kV. Tilting of the BNSL samples was carried out using a model 2040 dual-axis TEM tomography holder with the function of in-plane 360° rotation (Fischione Instruments). The tilting range of the holder is ±70° with respect to the high contrast pole piece of JEM1400. Scanning electron microscopy (SEM) was performed on a JEOL 7500F HRSEM. Three-dimensional structural models were built using Materials Studio 4.4 (Accelrys Software Inc.) and compared with the TEM images. Different projections were obtained by direct tilting of the built crystal structures. Electron diffraction simulation was performed with EMS software (Pierre Stadelmann). We also performed the two-dimensional Fourier transformation of the real-space TEM images to ensure consistency with the experimental small-angle electron diffraction patterns.

Supporting Information Available: Tilt series 6−9 of ico-AB_{13} BNSLs; additional TEM and SEM images of Fe_3O_4 nanocrystal assemblies; stereographic projection of hexagonal crystal system; media files showing the five tilt series of ico-AB_{13} BNSLs. This material is available free of charge *via* the Internet at http://pubs.acs.org.

REFERENCES AND NOTES

1. Murray, C. B.; Kagan, C. R.; Bawendi, M. G. Self-organization of CdSe nanocrystallites into three-dimensional quantum-dot superlattices. *Science* **1995**, *270*, 1335–1338.
2. Alivisatos, A. P. Semiconductor clusters, nanocrystals, and quantum dots. *Science* **1996**, *271*, 933–937.
3. Collier, C. P.; Saykally, R. J.; Shiang, J. J.; Henrichs, S. E.; Heath, J. R. Reversible tuning of silver quantum dot monolayers through the metal−insulator transition. *Science* **1997**, *277*, 1978–1981.
4. Murray, C. B.; Kagan, C. R.; Bawendi, M. G. Synthesis and characterization of monodisperse nanocrystals and close-packed nanocrystal assemblies. *Annu. Rev. Mater. Sci.* **2000**, *30*, 545–610.
5. Sun, S. H.; Murray, C. B.; Weller, D.; Folks, L.; Moser, A. Monodisperse FePt nanoparticles and ferromagnetic FePt nanocrystal superlattices. *Science* **2000**, *287*, 1989–1992.
6. Rabani, E.; Reichman, D. R.; Geissler, P. L.; Brus, L. E. Drying-mediated self-assembly of nanoparticles. *Nature* **2003**, *426*, 271–274.
7. Tang, Z. Y.; Zhang, Z. L.; Wang, Y.; Glotzer, S. C.; Kotov, N. A. Self-assembly of CdTe nanocrystals into free-floating sheets. *Science* **2006**, *314*, 274–278.
8. Nykypanchuk, D.; Maye, M. M.; van der Lelie, D.; Gang, O. DNA-guided crystallization of colloidal nanoparticles. *Nature* **2008**, *451*, 549–552.
9. Park, S. Y.; Lytton-Jean, A. K. R.; Lee, B.; Weigand, S.; Schatz, G. C.; Mirkin, C. A. DNA-programmable nanoparticle crystallization. *Nature* **2008**, *451*, 553–556.
10. Pileni, M. P. Supracrystals of inorganic nanocrystals: An open challenge for new physical properties. *Acc. Chem. Res.* **2008**, *41*, 1799–1809.
11. Cheng, W. L.; Campolongo, M. J.; Cha, J. J.; Tan, S. J.; Umbach, C. C.; Muller, D. A.; Luo, D. Free-standing nanoparticle superlattice sheets controlled by DNA. *Nat. Mater.* **2009**, *8*, 519–525.
12. Talapin, D. V.; Shevchenko, E. V.; Bodnarchuk, M. I.; Ye, X. C.; Chen, J.; Murray, C. B. Quasicrystalline order in self-assembled binary nanoparticle superlattices. *Nature* **2009**, *461*, 964–967.
13. Kiely, C. J.; Fink, J.; Brust, M.; Bethell, D.; Schiffrin, D. J. Spontaneous ordering of bimodal ensembles of nanoscopic gold clusters. *Nature* **1998**, *396*, 444–446.
14. Kalsin, A. M.; Fialkowski, M.; Paszewski, M.; Smoukov, S. K.; Bishop, K. J. M.; Grzybowski, B. A. Electrostatic self-assembly of binary nanoparticle crystals with a diamond-like lattice. *Science* **2006**, *312*, 420–424.
15. Redl, F. X.; Cho, K. S.; Murray, C. B.; O'Brien, S. Three-dimensional binary superlattices of magnetic nanocrystals and semiconductor quantum dots. *Nature* **2003**, *423*, 968–971.
16. Chen, Z. Y.; Moore, J.; Radtke, G.; Sirringhaus, H.; O'Brien, S. Binary nanoparticle superlattices in the semiconductor−semiconductor system: CdTe and CdSe. *J. Am. Chem. Soc.* **2007**, *129*, 15702–15709.
17. Overgaag, K.; Evers, W.; de Nijs, B.; Koole, R.; Meeldijk, J.; Vanmaekelbergh, D. Binary superlattices of PbSe and CdSe nanocrystals. *J. Am. Chem. Soc.* **2008**, *130*, 7833–7834.
18. Shevchenko, E. V.; Talapin, D. V.; O'Brien, S.; Murray, C. B. Polymorphism in AB_{13} nanoparticle superlattices: An example of semiconductor−metal metamaterials. *J. Am. Chem. Soc.* **2005**, *127*, 8741–8747.
19. Saunders, A. E.; Korgel, B. A. Observation of an AB phase in bidisperse nanocrystal superlattices. *ChemPhysChem* **2005**, *6*, 61–65.
20. Shevchenko, E. V.; Talapin, D. V.; Kotov, N. A.; O'Brien, S.; Murray, C. B. Structural diversity in binary nanoparticle superlattices. *Nature* **2006**, *439*, 55–59.
21. Shevchenko, E. V.; Talapin, D. V.; Murray, C. B.; O'Brien, S. Structural characterization of self-assembled multifunctional binary nanoparticle superlattices. *J. Am. Chem. Soc.* **2006**, *128*, 3620–3637.
22. Smith, D. K.; Goodfellow, B.; Smilgies, D.-M.; Korgel, B. A. Self-assembled simple hexagonal AB_2 binary nanocrystal superlattices: SEM, GISAXS, and defects. *J. Am. Chem. Soc.* **2009**, *131*, 3281–3290.
23. Shevchenko, E. V.; Talapin, D. V.; Rogach, A. L.; Kornowski, A.; Haase, M.; Weller, H. Colloidal synthesis and self-assembly of $CoPt_3$ nanocrystals. *J. Am. Chem. Soc.* **2002**, *124*, 11480–11485.
24. Cheon, J.; Park, J. I.; Choi, J. S.; Jun, Y. W.; Kim, S.; Kim, M. G.; Kim, Y. M.; Kim, Y. J. Magnetic superlattices and their nanoscale phase transition effects. *Proc. Natl. Acad. Sci. U.S.A.* **2006**, *103*, 3023–3027.
25. Urban, J. J.; Talapin, D. V.; Shevchenko, E. V.; Kagan, C. R.; Murray, C. B. Synergism in binary nanocrystal superlattices leads to enhanced p-type conductivity in self-assembled $PbTe/Ag_2Te$ thin films. *Nat. Mater.* **2007**, *6*, 115–121.
26. Zeng, H.; Li, J.; Liu, J. P.; Wang, Z. L.; Sun, S. H. Exchange-coupled nanocomposite magnets by nanoparticle self-assembly. *Nature* **2002**, *420*, 395–398.
27. Shevchenko, E. V.; Ringler, M.; Schwemer, A.; Talapin, D. V.; Klar, T. A.; Rogach, A. L.; Feldmann, J.; Alivisatos, A. P. Self-assembled binary superlattices of CdSe and Au nanocrystals and their fluorescence properties. *J. Am. Chem. Soc.* **2008**, *130*, 3274–3275.
28. Wang, Z. L. Structural analysis of self-assembling nanocrystal superlattices. *Adv. Mater.* **1998**, *10*, 13–30.
29. Wang, Z. L. New developments in transmission electron microscopy for nanotechnology. *Adv. Mater.* **2003**, *15*, 1497–1514.
30. Shoemaker, D. P.; Marsh, R. E.; Ewing, F. J.; Pauling, L. Interatomic distances and atomic valences in $NaZn_{13}$. *Acta Crystallogr.* **1952**, *5*, 637–644.
31. Haussermann, U.; Svensson, C.; Lidin, S. Tetrahedral stars as flexible basis clusters in sp-bonded intermetallic

frameworks and the compound $BaLi_7Al_6$ with the $NaZn_{13}$ structure. *J. Am. Chem. Soc.* **1998**, *120*, 3867–3880.

32. Murray, M. J.; Sanders, J. V. Close-packed structures of spheres of two different sizes. II. The packing densities of likely arrangements. *Philos. Mag. A* **1980**, *42*, 721–740.

33. Hachisu, S.; Yoshimura, S. Optical demonstratin of crystalline superstructures in binary mixtures of latex globules. *Nature* **1980**, *283*, 188–189.

34. Sanders, J. V. Close-packed structures of spheres of two different sizes. I. Observations on natural opal. *Philos. Mag. A* **1980**, *42*, 705–720.

35. Bartlett, P.; Ottewill, R. H.; Pusey, P. N. Superlattice formation in binary-mixtures of hard-sphere colloids. *Phys. Rev. Lett.* **1992**, *68*, 3801–3804.

36. Nagano, Y.; Nakamura, T. C_{60}-CCl_4 solvate: An AB_{13} type binary crystal. *Chem. Phys. Lett.* **1997**, *265*, 358–360.

37. Abbas, S.; Lodge, T. P. Superlattice formation in a binary mixture of block copolymer micelles. *Phys. Rev. Lett.* **2006**, *97*, 097803.

38. Friedrich, H.; Gommes, C. J.; Overgaag, K.; Meeldijk, J. D.; Evers, W. H.; de Nijs, B.; Boneschanscher, M. P.; de Jongh, P. E.; Verkleij, A. J.; de Jong, K. P. Quantitative structural analysis of binary nanocrystal superlattices by electron tomography. *Nano Lett.* **2009**, *9*, 2719–2724.

39. Williams, D. B.; Carter, C. B. *Transmission Electron Microscopy: A Textbook for Materials Science*; Plenum: New York, 1996; pp 267–287.

40. Eldridge, M. D.; Madden, P. A.; Frenkel, D. Entropy-driven formation of a superlattice in a hard-sphere binary mixture. *Nature* **1993**, *365*, 35–37.

41. Yethiraj, A.; van Blaaderen, A. A colloidal model system with an interaction tunable from hard sphere to soft and dipolar. *Nature* **2003**, *421*, 513–517.

42. Leunissen, M. E.; Christova, C. G.; Hynninen, A. P.; Royall, C. P.; Campbell, A. I.; Imhof, A.; Dijkstra, M.; van Roij, R.; van Blaaderen, A. Ionic colloidal crystals of oppositely charged particles. *Nature* **2005**, *437*, 235–240.

43. Bartlett, P.; Campbell, A. I. Three-dimensional binary superlattices of oppositely charged colloids. *Phys. Rev. Lett.* **2005**, *95*, 128302.

44. Park, J.; An, K. J.; Hwang, Y. S.; Park, J. G.; Noh, H. J.; Kim, J. Y.; Park, J. H.; Hwang, N. M.; Hyeon, T. Ultra-large-scale syntheses of monodisperse nanocrystals. *Nat. Mater.* **2004**, *3*, 891–895.